Clays and Clay Minerals, Vol. 66, No. 3, 261–273, 2018.

EFFECTS OF Fe AND V STATES ON THE FENTON CATALYTIC ACTIVITY OF NATURAL RUTILE

YANZHANG LI[1,§], ZEMIN LUO[1,2,§], YAN LI[1,*], FEIFEI LIU[1], ANHUAI LU[1], JING WU[1], SHAN QIN[1], AND CHANGQIU WANG[1]

[1] The Key Laboratory of Orogenic Belts and Crustal Evolution, Beijing Key Laboratory of Mineral Environmental Function, School of Earth and Space Sciences, Peking University, Beijing 100871, PR China

[2] Center for Innovative Gem Testing Technology, Gemological Institute, China University of Geosciences, Wuhan 430074, PR China

Abstract—As a common mineral phase on Earth and Martian regolith, natural rutile was reported as a potential candidate for use as a Fenton catalyst in this study. The influences of Fe and V in various chemical states on the generation of reactive oxygen species (ROSs) and the catalytic activity of rutile were examined. A series of rutile samples with various surface and bulk states of Fe and V were obtained initially by hydrogen annealing of natural rutile at ~773−1173 K. X-ray diffraction, electron paramagnetic resonance spectra, and X-ray photoelectron spectroscopy demonstrated that the atomic fractions of Fe(III) and V(V) decreased sharply with increasing temperature, along with the accumulation of surface Fe(II) and bulk V(III). All as-prepared materials showed enhanced Fenton degradation efficiency on methylene blue (MB) compared with P25-TiO_2, and the treated samples exhibited up to 3.5-fold improvement in efficiency at pH 3 compared to the untreated sample. The improved efficiency was attributed mainly to Fenton catalysis involving Fe(II) and V(III). The dissolved Fe^{2+} played a crucial role in the homogeneous Fenton reaction, while the bound V(III) favored adsorption primarily and may have facilitated heterogeneous Fenton reaction and the regeneration of Fe^{2+}. The pH regulated the reaction mechanism among homogeneous (pH = 3) and heterogeneous (pH = 3.7) Fenton catalysis and physical adsorption (pH = 5, 6). The aim of the present study was to improve the understanding of the potential role of natural rutile with advanced oxidation functions in Earth systems and even on Mars, which also provide an inspiration for screening natural rutile and any other similar, Earth-abundant, low-cost minerals for environmental application.

Key Words—Fe and V co-doping, Fenton reaction, Heterogeneous catalysis, Homogeneous catalysis, Hydrogen annealing, Natural rutile.

INTRODUCTION

Natural minerals enjoy many inherent virtues such as large abundance, great variety, low cost, ready availability, and no secondary pollution, making them suitable for large-scale industrial and commercial applications. Natural minerals have also been found to have some environmentally friendly properties in terms of pollutant purification, including surface adsorption (Liang *et al.*, 2010; Uddin, 2017), porous filtration (Dong *et al.*, 2006; Gülay *et al.*, 2014), ionic exchange and immobilization (Griffin *et al.*, 1977; Tekbaş *et al.*, 2008; Gómez-Hortigüela *et al.*, 2014), chemical catalysis such as photocatalysis (Lu *et al.*, 2007; Xia *et al.*, 2013; Li *et al.*, 2018), and Fenton reactions (Matta *et al.*, 2008; Pereira *et al.*, 2012; Xia *et al.*, 2017), as well as mineral−bacteria interactions (Lu *et al.*, 2012; Shi *et al.*, 2016). Of all of the above properties, Fenton and Fenton-like reactions are very efficient and have almost no selectivity towards oxidization (Pignatello *et al.*, 2006; Liang *et al.*, 2010; Xia *et al.*, 2017), and thus are very desirable in terms of dealing with severe contamination situations (Pignatello *et al.*, 2006; Matta *et al.*, 2008; Pereira *et al.*, 2012; Laiju *et al.*, 2014). In practice, homogeneous Fenton reactions are active in terms of removing pollutants in bulk solution and heterogeneous Fenton reactions at the mineral surface−liquid interface. In both cases, the catalytic performance is related to the existing states of transition metals in minerals, such as Fe, V, Ti, Cr, Mn, *etc.* (Liang *et al.*, 2010; Pereira *et al.*, 2012; Liang *et al.*, 2013).

Natural rutile (TiO_2) is one of the most common minerals on the Earth's surface and is the most resistant to weathering, always associated with clays, quartz, and feldspar in soil (Jackson *et al.*, 1948; Allen and Hajek, 1989; Wang *et al.*, 2013; Mehmood *et al.*, 2015). Even certain clay deposits, *e.g.* kaolinite, illite, and bentonite, contain rutile-type TiO_2 (Dolcater *et al.*, 1970; Sayin *et al*., 1975). Natural rutile was found to exist in Martian soil regolith as well as in the subsurface at an abundance of 0.5−2 wt.% (Baird *et al*., 1976; Rieder *et al*., 1997; Ming *et al*., 2008). As for all natural minerals, complex geological environments endow natural rutile with inherent defects in the form of substituting and interstitial metal ions, vacancies, *etc*. Among them, Fe and V are the two most common substituting metals and always

* E-mail address of corresponding author:
liyan-pku@163.com
DOI: 10.1346/CCMN.2018.064091
§ The first two authors contributed equally to this paper

coexist in rutile crystals (Suzuki and Pavasupree, 2005). Natural Fe- and V-containing rutile has been found to be a cost-effective and environmentally friendly mineral photocatalyst (Lu *et al.*, 2004., 2007; Chuan *et al.*, 2008), but, to date, its Fenton effect has not been reported. The oxidation states of Fe and V are relevant to the Fenton catalytic activity of Fe- or V-doped minerals, such as different kinds of Fe (oxyhydr)oxides and V-doped magnetite according to Pereira *et al.* (2012) and Liang *et al.* (2010a, 2010b, 2013). Taking into account the complexity of the ore-forming environment, *e.g.* fluid, temperature, and redox potential, the chemical states of originally doped Fe and V in natural rutile from different deposits cannot be the same. Accordingly, rutile samples from different deposits, or which have experienced different weathering actions, should exhibit different catalytic activities, especially in Fenton or Fenton-like reactions. To screen for the most appropriate natural rutile candidate to apply to degradation of pollutants, and to reveal how the surface states of transition metals impact on the environmental functions of rutile in soils, investigation of the influences of the chemical states of Fe and V on the Fenton catalytic activity of rutile is required.

The objectives of the present study were, therefore, to investigate how the diverse states of surface and bulk Fe and V in natural rutile influence its Fenton reaction efficiency. An opportunity was also provided to screen for natural minerals with potential practical value and cost advantages in environmental remediation represented by rutile and its treated products. Moreover, the results revealed here will also help to propose an alternative mechanism of yielding reactive oxygen species (ROSs) by rutile Fenton catalysis on Mars.

MATERIALS AND METHODS

Natural material

The natural rutile sample used in the present study was collected from a metamorphism-alteration deposit in Shanxi Province, China. This natural rutile sample, referred to hereafter as untreated rutile, was ground to an average particle size of <74 μm. The general chemical composition of this rutile was $(Ti_{0.988}V_{0.010}Fe_{0.004})_{1.002}O_2$, as determined using a JXA-8100 electron microprobe (JEOL Ltd., Tokyo, Japan) (Luo *et al.*, 2012).

Preparation of hydrogen-annealed rutile samples

The untreated rutile in an alumina porcelain boat was loaded into a Lindberg/Blue M high-temperature tubular furnace (Thermo Fisher Scientific, Waltham, Massachusetts, USA) equipped with a vacuum pump. The process of creating vacuum (<3.0 Pa) in the furnace and reloading protective argon (Ar) gas was repeated three times. The sample was heated from room temperature (298 K) to the desired annealing temperature (773 K, 873 K, 973 K, 1073 K, or 1173 K, respectively) with a continuous gas flow (10% H_2/Ar) of 200 mL/min and temperature ramp rate of 15 K/min. During the annealing treatment process, the pressure of the system was maintained at 1.0 atm. After 3 h of annealing, the sample was cooled to room temperature naturally under the Ar atmosphere. The hydrogen-annealed rutile samples are referred to hereafter (with reference to their annealing temperatures) as H_2-773, H_2-873, H_2-973, H_2-1073, and H_2-1173. The cooled samples were then transferred quickly (several minutes) to an anaerobic glove box filled with Ar gas to avoid oxidation.

Characterization techniques

Powder X-ray diffraction (XRD) patterns of rutile samples were recorded using a D/max-rA diffractometer (Rigaku Industrial Corporation, Tokyo, Japan) using CuKα radiation at a scanning speed of 0.5º2θ/min. The accelerating voltage and applied current were 40 kV and 100 mA, respectively. To detect the valence states and local geometric structures of dopant cations, electron paramagnetic resonance spectra (EPR) of untreated rutile and hydrogen-annealed powdered samples with a uniform mass of 0.02 g were measured at liquid nitrogen temperature (77 K) using a JES-FA200 spectrometer (JEOL Ltd., Tokyo, Japan). The spectra were recorded as first-derivative plots at a microwave frequency of 9.1 GHz (X-Band) and power of 1.0 mW. A signal of Mn(II) was used as an internal standard. The X-ray photoelectron spectroscopy (XPS) measurements were carried out using an AXIS Ultras instrument (Kratos Analytical Ltd, Manchester, UK) with AlKα source (1486.6 eV) to obtain the surface characteristics of dopant ions in rutile samples. The C 1s peak at 284.8 eV served as an internal reference for the calibration of absolute binding energy and all the data were processed using the *CasaXPS* software package (version 2.3.16, Casa Software Ltd., Teignmouth, UK).

MB degradation experiments

As a model simulated pollutant, methylene blue (MB) degradation experiments were launched to test the pollutant-removal efficiency of untreated rutile and treated samples. Reactants were combined in an Erlenmeyer flask with a final total volume of 100 mL of suspension in concentrations of 5 mg/L of MB, 1.0 g/L of powdered sample, and 8.8 mmol/L of hydrogen peroxide (H_2O_2). The initial pH values were set at some arbitrary points and adjusted by adding HCl or NaOH. Each flask was wrapped in aluminum foil to avoid any influence of light. The reaction system was stirred continuously for 2 h. At 30 min intervals, a 10 mL suspension (10.05 g) was withdrawn from each flask and centrifuged (9900 r/min for 10 min). The MB concentration in the supernatant was determined using an HP-8453 UV-visible spectrophotometer (Agilent,

https://doi.org/10.1346/CCMN.2018.064091 Published online by Cambridge University Press

Santa Clara, California, USA) at the maximum absorbance wavelength of MB (664 nm). The removal rate of MB was calculated using the following formula:

$$\text{Removal rate (\%)} = (1 - C_t / C_o) \times 100\% \quad (1)$$

where C_0 is the initial concentration of the dye solution and C_t is the concentration of the dye solution at time t.

Measurement of leached Fe and V ions

The concentrations of Fe^{2+} and total Fe ions leached in solution were measured using the 1,10-phenanthroline spectrophotometric method (Kremer, 2008; Shimizu *et al.*, 2012). Optical absorption was measured at the wavelength of 510 nm (using the aforementioned spectrophotometer), which was the maximum absorption peak of the Fe^{2+}-σ-phenanthroline complex. The experimental conditions were the same as above except that MB was not added in order to avoid color interference in the chromogenic reaction of Fe^{2+} with 1,10-phenanthroline. After 30 min of stirring, 10 mL of suspension (10.05 g) was removed and centrifuged. Then, the supernatant was subdivided into three equal parts, each of which was used to measure the concentration of Fe^{2+}, total Fe ions, and V ions. The total Fe ions were all reduced to Fe^{2+} in the presence of hydroxylamine hydrochloride ($NH_2HO{\cdot}HCl$) before adding 1,10-phenanthroline. Inductively Coupled Plasma-Atomic Emission Spectrometry (ICP-AES, Teledyne Leeman Labs, Hudson, New Hampshire, USA) was performed to detect the quantity of total dissolved V ions in the reaction solution.

All of the chemicals used in the present study were of analytical purity grade and obtained from Sinopharm Chemical Reagent Co., Ltd, Shanghai, China, including H_2O_2 (30%, V%), methylene blue ($C_{16}H_{18}N_3SCl{\cdot}3H_2O$), HCl (36%, V%), sodium hydroxide (NaOH), 1,10-phenanthroline ($C_{12}H_8N_2{\cdot}H_2O$), and hydroxylamine hydrochloride ($NH_2HO{\cdot}HCl$). P25-TiO_2 was purchased from Degussa AG (Frankfurt, Germany). All solutions were prepared at room temperature with 18.2 MΩ·cm Mill-Q ultrapure water.

RESULTS AND DISCUSSION

Mineral phase changes with the annealing temperature

All of the diffraction peaks in the XRD patterns (Figure 1 and inset) were assigned to the phase of rutile-TiO_2 (JCPDS 89-4920) except for an additional diffraction peak (44.6º2θ) for high-temperature-annealed samples (H_2-1073 and H_2-1173). This peak, indicated with an arrow, was assigned to the strongest diffraction peak of zero-valence metallic iron (Fe^0) for the crystal face (110) (JCPDS 89-7194). The formation of Fe^0 indicated that Fe in untreated rutile had been reduced to lower valence states (<+3) after hydrogen treatment. Nevertheless, rutile was still the main mineral phase before and after the treatment.

Variation of Fe and V in surface and bulk states

EPR. The mass fractions of Fe and V in the rutile samples as shown by EMPA results were 0.4 wt.% and 1.0 wt.%, respectively (Luo *et al.*, 2012). For such low dopants, EPR is the most effective technique for determining the valence states, occupied sites, and local symmetries of Fe(III), Fe(II), V(IV), V(III), and V(II) due to the existence of unpaired electrons (Occhiuzzi *et al.*, 2003; Gopal *et al.*, 2004). Each EPR

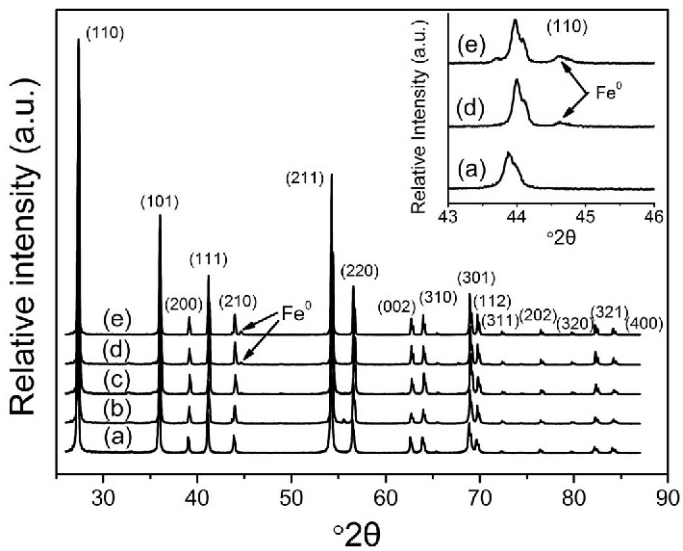

Figure 1. XRD traces of untreated rutile and hydrogen-annealed samples: (a) untreated rutile, (b) H_2-873, (c) H_2-973, (d) H_2-1073, (e) H_2-1173. The arrows indicate the (110) crystal face of iron (enlarged in inset image, upper right). The XRD trace of H_2-773 is not shown.

https://doi.org/10.1346/CCMN.2018.064091 Published online by Cambridge University Press

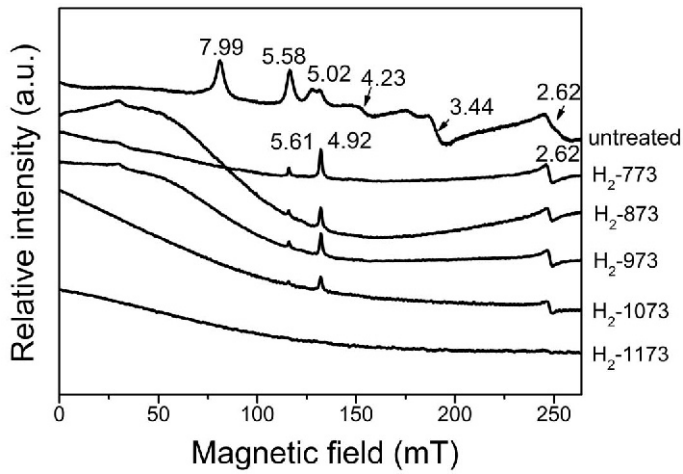

Figure 2. EPR spectra of untreated rutile and hydrogen annealed samples recorded in the magnetic field from 0 to 260 mT. The g values labeled in the figure correspond to EPR signal peaks caused by Fe(III) located in various symmetry sites in rutile-TiO_2.

signal of Fe(III) in untreated rutile and hydrogen annealed samples (Figure 2) was assigned to the local structure of Fe(III) based on the differences in g-values (Table 1). For untreated rutile, Fe(III) was the main state and Fe(III) symmetry sites had two types. First, the signal at g = 4.23 was typical of an isolated rhombic Fe(III) cation in a high-spin configuration with a strong distorted environment (E/D = 1/3) (Thorp and Eggleston, 1985; Soria *et al.*, 1991; Egerton *et al.*, 2001; Pecchi *et al.*, 2003; Chakradhar *et al*., 2006). Here D and E are the axial and rhombic component parameters of the crystal field, respectively. The second group with peaks at g = 7.99, 5.58−5.02, 3.44, and 2.62 in untreated rutile correspond to signals for substituting Fe(III) with a relatively lower rhombic distortion (Amorelli *et al.*, 1987; Soria *et al.*, 1991; Pecchi *et al*., 2003).

After hydrogen annealing, only three peaks (g = 5.61, 4.92, and 2.62) remained for the modified samples (H_2-773, H_2-873, H_2-973, and H_2-1073), the intensities of which decreased sharply. Compared with natural rutile, the narrower and more symmetrical EPR peaks implied that the substituting Fe(III) should be located at a more stable crystal structure, indicating that high temperature probably enhanced the mineral crystallinity. In addition, the vanishing of EPR signals and decline of intensities with the increasing temperature suggested the decrease of unpaired electrons outside the Fe electron-shell, which could be ascribed to Fe(III), was gradually reduced to lower valence states, *i.e.* Fe(II) and Fe^0. In terms of H_2-1173, no EPR signal was detected except a curved baseline over the entire range of magnetic field, attributed to the formation of Fe(II) and Fe^0, both of which are silent in conventional EPR measurement (Knapp *et al.*, 2000).

EPR signals of vanadium in untreated rutile and hydrogen-annealed samples (Figure 3) revealed that all the samples except H_2-1073 and H_2-1173 exhibited an obvious eight-fold hyperfine splitting structure. The calculated g and A (the hyperfine coupling constants) values ($g_{//}$ = 1.98, $g_{\perp}$ = 1.93, $A_{//}$ = 15.4 (mT), and $A_{\perp}$ = 4.1 (mT)) were very close to that of substituting V(IV) in rutile (Gallay *et al.*, 1986; Kera and Matsukaze, 1986; Cavani *et al.*, 1988; Rodella *et al.*, 2002; Tian *et al.*, 2009). For untreated rutile, judging from the weak EPR signal of V(IV), V(V) could be the main state of V accompanying the small amount of V(IV), which were demonstrated in detail in previous work (Luo *et al.*,

Table 1. EPR signal assignments for the untreated rutile and hydrogen-annealed samples in the magnetic range from 0 to 260 mT (Thorp and Eggleston, 1985; Amorelli *et al.*, 1987; Soria *et al.*, 1991; Egerton *et al.*, 2001; Pecchi *et al.*, 2003; Chakradhar *et al*., 2006).

Sample	Experiment g value	Assignment
Untreated rutile	4.23	Fe(III) located in a strong distorted rhombic symmetry site (E/D = 1/3)
	7.99, 5.58, 5.02, 3.44, 2.62	Fe(III) substituted for Ti(IV) in the rutile crystal lattice with less rhombic distortion
H_2-773, H_2-873, H_2-973, H_2-1073	5.61, 4.92, 2.62	Fe(III) substituted for Ti(IV) in the rutile crystal lattice at a more stable structure

https://doi.org/10.1346/CCMN.2018.064091 Published online by Cambridge University Press

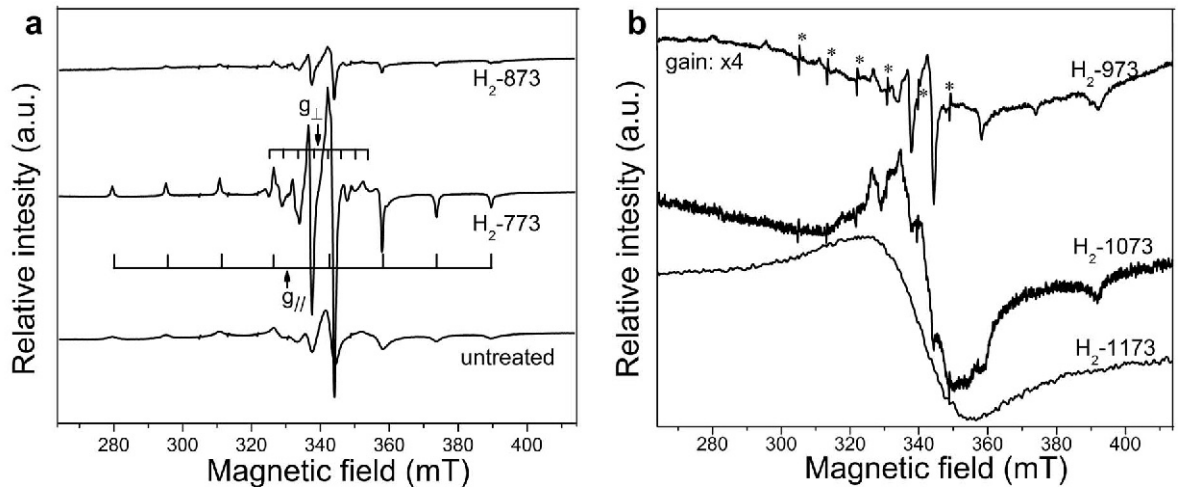

Figure 3. (a) EPR spectra of untreated rutile, H_2-773, and H_2-873; (b) EPR spectra of H_2-973, H_2-1073, and H_2-1173 with $\times 4$ magnification recorded in the magnetic field from 264 to 500 mT. The * symbol represents the signal from the internal Mn(II) standard. The $g_{//}$ and $g_{\perp}$ marked on the figure correspond to eight-fold hyperfine splitting structure lines of V(IV).

2012). After hydrogen annealing, the intensity of signal assigned to V(IV) notably strengthened in the H_2-773 sample, but then diminished sharply in H_2-873 and H_2-973 with the rising temperature. In the case of the H_2-1073 sample, the eight-fold hyperfine splitting structure could not be identified clearly due to the low intensity. For H_2-1173, the eight-fold hyperfine splitting structure had disappeared completely, which could result from the formation of V(III) which had no EPR signal, as for Fe(II) (Brückner, 2006). Based on the discussion above, the substantial increase in V(IV) at 773 K was due to the reduction of V(V) and then V(IV) gradually converted to V(III) above 773 K.

Under the present experimental conditions (77 K, X-band, microwave frequency (~9.5 GHz)), neither Fe(II) nor V(III) was detected directly because they displayed considerable zero-field splitting (ZFS) due to the absence of unpaired electrons ($3d^6$, $3d^2$) (Knapp *et al.*, 2000; Brückner, 2006). Their signals can only be observed by high-frequency, high-magnetic field EPR or dual-mode EPR. Their existence and variation tendency, however, could be inferred through the vanishing signals of Fe(III) and V(IV).

XPS. X-ray photoelectron spectroscopy is a means of detecting the surface chemical states of Fe, V, Ti, and O in rutile samples, as well as the atomic ratio, at nano-depths (up to 10 nm). The core-level XPS spectra of Fe 2p in untreated rutile and some treated samples (Figure 4) showed that the binding energy values centered at ~709.0 eV and 722.6 eV (blue fitted lines) were assigned to Fe(II), and those at 711.0 eV and 724.6 eV (green fitted lines) were assigned to Fe(III) (Yamashita and Hayes, 2008). In addition, some satellite peaks, caused by Fe 3d − O 2p hybridization, appeared at ~714.7 eV (blue line) and 718.8 eV (green line) corresponding to Fe(II) and Fe(III), respectively (Fujii *et al.*, 1999; Yamashita and Hayes, 2008). As the temperature increased, the Fe(II) signal strengthened and this could be interpreted as an increase in Fe(II) as a proportion of total Fe. The XPS signals of Fe^0 should emerge at Fe $2p_{3/2}$ = 706.9 eV and Fe $2p_{1/2}$ = 719.9 eV, but these were undetected in all samples (Fiedor *et al.*, 1998; Geng *et al.*, 2009). This phenomenon might be due to the tiny particle size, small content, and uneven distribution of Fe^0, making it difficult to detect. Based on the integrated area of Gaussian-resolved peaks and the sensitivity factor for Fe (Wagner, 1983), the atomic fractions of Fe(II) and Fe(III) in the detected volume under different conditions were obtained (Table 2). The ratio of surface Fe(II)/Fe(III) remained relatively stable at ~0.3 in the lower annealing temperature range

Table 2. Surface Fe species (at.%) in rutile samples.

Chemical states	Untreated	H_2-773	H_2-873	H_2-973	H_2-1073	H_2-1173
Fe(II)	0.32	0.48	0.50	0.64	0.58	0.09
Fe(III)	0.95	1.65	1.74	1.24	0.54	0.11
Σ(Fe(II) + Fe(III))	1.27	2.13	2.24	1.88	1.12	0.20
Fe(II)/Fe(III)	0.34	0.29	0.29	0.52	1.07	0.82

https://doi.org/10.1346/CCMN.2018.064091 Published online by Cambridge University Press

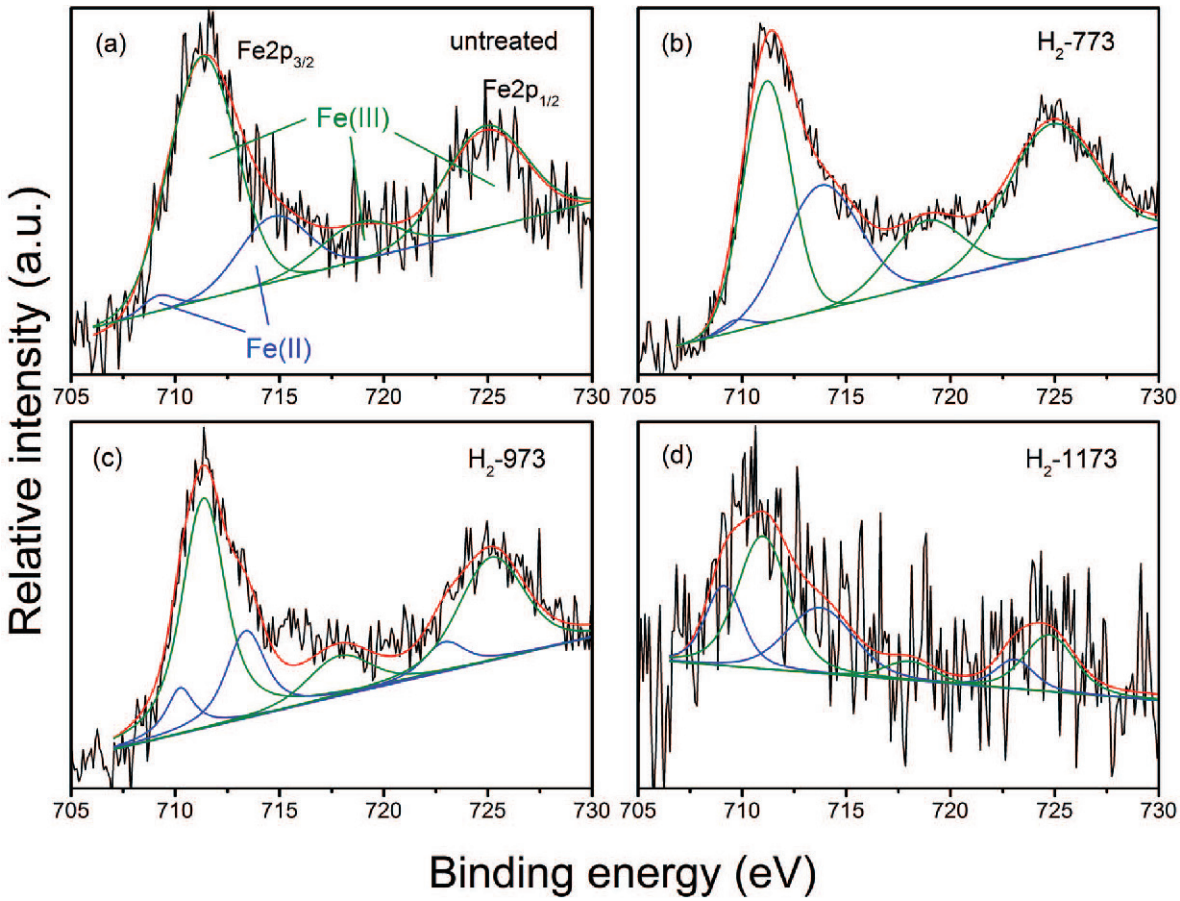

Figure 4. Fe 2p core-level XPS spectra of some rutile samples. The black lines were experimental data with poor signal-to-noise ratio due to low content. The blue and green lines are fitted peaks of Fe(II) and Fe(III), respectively. The red lines represent simulative curves based on fitted results.

($T \leqslant 873$ K), but began to increase (>0.5) at higher temperatures ($T \geqslant 973$ K). This considerable change suggested that the surface Fe(III) was reduced to Fe(II). Note that the total atomic fraction of surface Fe(II) and Fe(III) in hydrogen-annealed samples, *i.e.* H_2-773 (2.13 at.%), H_2-873 (2.24 at.%), and H_2-973 (1.88 at.%), were obviously greater than that of the untreated rutile (1.27 at.%), indicating the migration of Fe from the bulk to the surface in high-temperature-treated samples. As for H_2-1073 and H_2-1173, the substantial decrease of total ionic Fe might be due to the formation of Fe^0, according to the XRD results. Combining with the EPR results, the conclusion is that both surface and bulk Fe(III) were reduced almost entirely to Fe(II) and Fe^0 at 1173 K.

As for surface V states, no observable V-related signal was detected in untreated rutile but weak signals were found in hydrogen-annealed samples (Figure 5). Although the mass fraction of V in the original rutile sample was 1.5 times greater than Fe (Luo *et al.*, 2012), the atom percentage of surface V (0.3 at%) detected in all treated samples was much lower than that of Fe (1.0 at.%). The V atoms, therefore, preferred to stay in the bulk rather than at the surface site, even after high-temperature annealing. Under high temperature and the reducing atmosphere of hydrogen, only a few V species could migrate towards the surface. After smoothing and fitting processes (red curves in Figure 5), the peak centers and assignment of binding energy values to V $2p_{3/2}$ were obtained (Table 3). All treated samples exhibited very weak peaks centered from 516.5 eV to 515.7 eV, which were assigned to the valence of V from V(V) to V(III) (Sawatzky and Post, 1979; Wagner, 1979; Luo *et al.*, 2012). Note that neither a V(II) nor a V(I) signal was observed in samples for which the V $2p_{3/2}$ binding energy values were <515 eV, implying that V(III) was the terminal state of the hydrogen-modified rutile series. The binding energy values for V $2p_{3/2}$ decreased gradually with elevated temperature, which confirmed that V underwent reduction reactions. Another interesting phenomenon was that the XPS results showed that 1073 K was the temperature at which surface V(III) formed, but the EPR results implied that V(III) might start to appear at 873 K. The difference here was attributed to the fact that XPS was able to obtain just the elementary information at the surface,

https://doi.org/10.1346/CCMN.2018.064091 Published online by Cambridge University Press

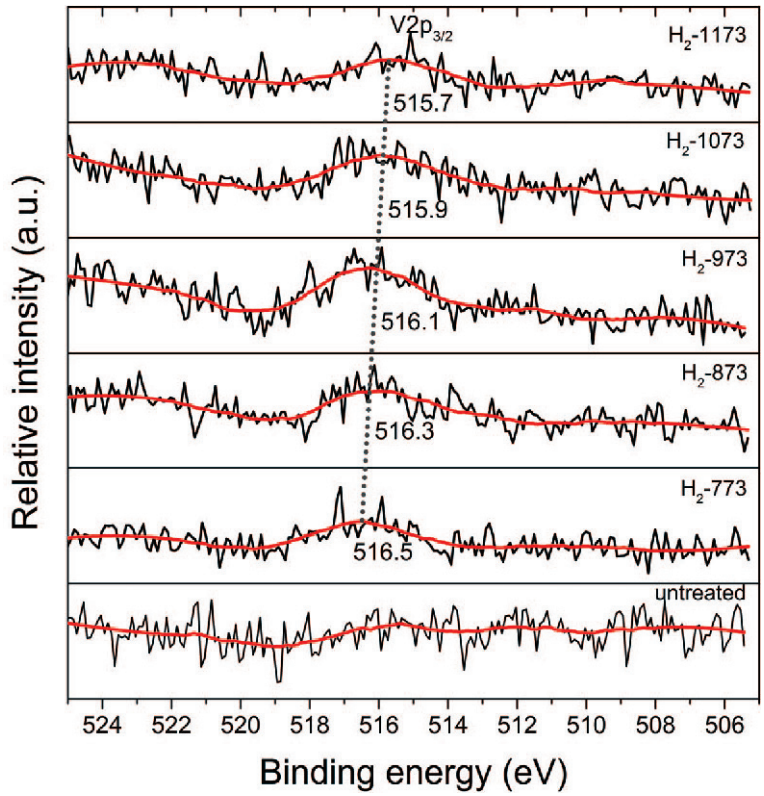

Figure 5. V $2p_{3/2}$ core-level XPS spectra of all rutile samples, under various treatment conditions. The solid black lines represent the experimental spectra and the red solid lines, the smoothed curves. The dotted black line connects the crest of every curve demonstrating the changing trend of oxidation states, *i.e.* from V(V) to V(III).

while EPR demonstrated the valence-state information at the surface and in bulk. This result showed that V(III) produced at 873 K would not be present at the surface of sample until the temperature reached 1073 K, further indicating that V(III) could migrate from bulk to surface gradually from 873 K to 1073 K. The different behaviors of V and Fe might be related to their chemical mobility and diffusivity.

In addition, the surface chemical states of Ti and oxygen vacancy throughout the whole reduction process should lead to other concerns. Surprisingly, Ti(IV) was the only observed Ti state (Figure S1 in Supplementary Material, available from http://www.clays.org/Journal/JournalDeposits.html) and the atomic fraction of oxygen vacancy didn't change much in any rutile samples (Figure S2 and Table S1 in Supplementary Material). Another problem was how V(V) was reduced to V(III) when most V did not really exist at the surface sites and could scarcely be reduced by hydrogen directly. In fact, these problems are attributed to the same issue. The reduction of V(V) in the bulk phase could benefit from a small amount of Ti(III) which was first reduced by hydrogen on the rutile surface. Then, charge transfer occurred from surface to bulk through linkages of V-O-Ti, followed by subsequent reduction of V(V) and regeneration of Ti(IV) (Trifir, 1998; Klosek and Raftery, 2001; Bhattacharyya *et al.*, 2008). Such a process is referred to as inter-valence charge transfer (IVCT) and is described in equation 2. Besides, the ability of Fe(III) to accept electrons was greater than that of Ti(IV) and similar IVCT could help to minimize the reduction of Ti(IV), as is expressed in equation 3 (Seki

Table 3. V $2p_{3/2}$ binding energy values and corresponding valences for all rutile samples.

	Samples					
	Untreated	H_2-773	H_2-873	H_2-973	H_2-1073	H_2-1173
Peak center (eV)	–	516.5	516.3	516.1	515.9	515.7
Assigned valence	–	V(V), V(IV)	V(IV)	V(IV)	V(IV), V(III)	V(III)

–: No V XPS signal was detected in the untreated samples.

https://doi.org/10.1346/CCMN.2018.064091 Published online by Cambridge University Press

et al., 2005). The absence of Ti(III) could further avoid oxygen atoms escaping from the lattice, maintaining them in the $Ti(IV)O_6$ octahedron. In this regard, V(V) and Fe(III) could serve as a coupled redox buffer to keep the stability of the rutile phase even in severely reduced conditions.

$$Ti(III) + V(V) \rightarrow V(IV) + Ti(IV) \quad (2)$$

$$Ti(III) + Fe(III) \rightarrow Fe(II) + Ti(IV) \quad (3)$$

According to EPR and XPS results, Fe(III) and V(V) were the predominant impurity cations in untreated rutile. After hydrogen annealing, on one hand, a predictable tendency was observed that Fe(III) migrated gradually from the bulk to the surface and was concurrently reduced to lower oxidation states, *i.e.* Fe(II) and Fe^0. On the other hand, V(V) was also transformed into V(IV) and V(III) after hydrogen treatment, but they were located mainly in the bulk rather than at the surface. Based on the above discussion, the main thermal chemical reactions during the hydrogen annealing process are summarized as follows in equations 4 and 5:

873–1073 K:

$$(Ti_{0.988}(V^{V},V^{IV})_{0.01}Fe^{III}_{0.004})_{1.002}O_2 + H_2 \rightarrow (Ti_{0.988}(V^{IV},V^{III})_{0.01}Fe^{II}_{x}Fe^{III}_{0.004-x})_{1.002}O_2 \quad (4)$$

1173 K:

$$(Ti_{0.988}(V^{IV},V^{III})_{0.01}Fe^{II}{}_{x}Fe^{III}_{0.004-x})_{1.002}O_2 + H_2 \rightarrow (Ti_{0.988}V^{III}_{0.01}Fe^{II}_{0.004-y})O_2 + yFe^0 \quad (5)$$

where x and y represent the ratio of newly formed Fe(II) and elemental Fe, respectively ($0<x<0.004$, $0<y<0.004$).

MB degradation efficiency by hydrogen-annealed samples

The MB was used as a simulated pollutant to check the chemical activity of all prepared rutile samples as well as P25-TiO_2 and a blank control (no catalyst) (Figure 6). The removal of MB in the blank control was negligible whether H_2O_2 was added or not; in contrast, rutile samples worked well for the removal of MB. In the system with H_2O_2 at pH = 3.0, the untreated rutile sample showed a much greater rate of degradation of MB (27.4%) than did P25-TiO_2 (4.7%). Because no substituting transition metal cation was found in P25-TiO_2, the result implied that the substituting Fe and V in the rutile sample played a key role in MB degradation. In addition, compared to untreated rutile, the hydrogen-annealed rutile samples displayed a significantly enhanced removal rate of MB as the annealing temperature increased from 773 K to 1173 K (illustrated as black columns in Figure 6). The two highest-temperature annealed samples (H_2-1073 and H_2-1173) showed a ~2.5 times greater MB-removal rate than that of untreated rutile, suggesting samples with lower-valence metal species (Fe(II) and V(III)) favored promotion of reaction activities. Compared to H_2-1073, the MB degradation efficiency by H_2-1173 decreased slightly, which could be ascribed to the reduction of total electrovalent Fe in H_2-1173 due to the formation of Fe^0.

The physical adsorption of MB in the absence of H_2O_2 was achieved in parallel (gray columns in Figure 6). The adsorption rates of all samples after 2 h were <20%. The same tendency was exhibited as for those systems with H_2O_2, *i.e.* the lower the valence state of the cations, the greater the removal efficiencies they

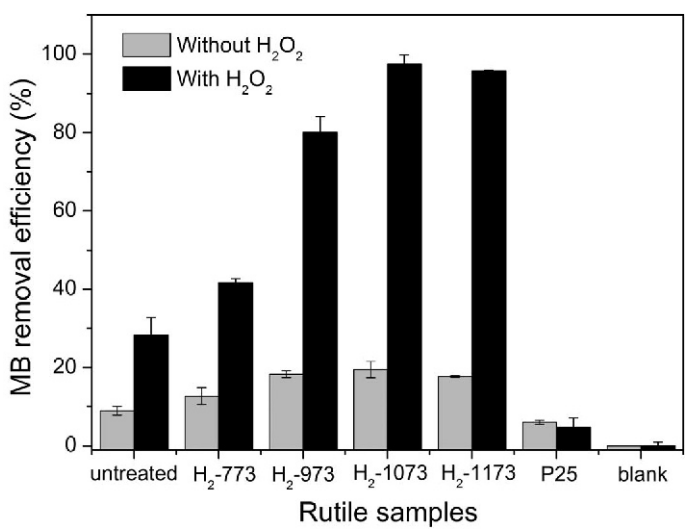

Figure 6. MB-removal efficiencies under multiple experiment conditions (black and gray columns represent reaction systems with and without H_2O_2, respectively) for untreated rutile and hydrogen samples annealed at various temperatures, as well as P25-TiO_2 and a blank control (in the absence of catalyst). The total reaction time was 2 h. Composition of reaction mixture (100 mL final volume): sample, 1.0 g/L; initial MB concentration, 5.0 mg/L; H_2O_2 concentration, 8.8 mmol/L; initial pH: 3.

https://doi.org/10.1346/CCMN.2018.064091 Published online by Cambridge University Press

had. In particular, P25-TiO_2 showed the worst adsorption performance even though it had a large surface area and good adsorption capability. The results not only confirmed the improved degradation capability towards MB of natural rutile and its treated samples in the presence of H_2O_2, but also suggested that those surface V and Fe cations were indeed considerable factors in the adsorption of MB molecules. In conclusion, the decrease in MB concentration should be due mainly to the chemical reaction which occurred between Fe/V co-doped rutile samples and H_2O_2, as well as physical adsorption.

Discussion of the roles of Fe(II) and V(III)

According to the experimental results above, the enhanced MB degradation rate could be attributed to the combined effect of H_2O_2 and cation-bearing materials. This complies exactly with the characteristics required for Fenton reaction in which H_2O_2 is converted to a hydroxyl radical (·OH) in the presence of reduced-state cations (Liang *et al.*, 2010; Pereira *et al.*, 2012; Liang *et al.*, 2013). In order to verify how Fe and V got involved in this reaction, it was necessary to measure their corresponding dissolved cations. In the experimental solution after 0.5 h, measurement results (Table 4) showed that the concentration of Fe^{2+} and Fe^{3+} in the solution of H_2-1173 system were ~3 and ~4 times greater than that of untreated rutile, respectively. Clearly, the dissolved Fe^{2+} could react with H_2O_2 and further produce Fe^{3+} and ·OH; the latter had powerful oxidizing ability to degrade organic pollutants (Wang, 2008). This is a so-called homogeneous Fenton reaction and is the primary reason for the high rate of MB degradation by sample H_2-1173, according to equation 6:

$$Fe^{2+}_{aq} + H_2O_2 \rightarrow Fe^{3+}_{aq} + \cdot OH + OH^-, \quad E_0 = 0.528 \text{ V (at pH = 3)} \qquad (6)$$

The concentration of dissolved V ions in each suspension after reaction, however, was below the detection limit (ppb level), indicating that hardly any V ion was leached out. As mentioned above, the adsorption effect was enhanced for the treated sample which was due to the fact that the atomic fractions of surface Ti(IV) and oxygen vacancy remained constant, and to the considerable leaching of Fe ions. The stable bonding of V on the surface of rutile, especially V(IV) and V(III) in H_2-973, H_2-1073, and H_2-1173 should, therefore, play an important role in physical adsorption. The incorporation of V in $Fe_{3-x}V_xO_4$ magnetite may promote the adsorption of MB (according to Liang *et al.*, 2010), and the same mechanism could indicate that V on the surface of rutile promoted the adsorption. Besides, the redox potentials for H_2O_2/H_2O, Fe(III)/Fe(II), and V(IV)/V(III) are 1.299 V, 0.771 V, and 0.337 V (*vs.* NHE in pH = 3), respectively (Bossmann *et al.*, 1998; Liang *et al.*, 2010). Thus, thermodynamics favored H_2O_2 first oxidizing surface V(III) rather than Fe(II). This so-called heterogeneous Fenton reaction took place exactly at the interface between the solid surface and the liquid, which is described in equation 7. Meanwhile, V(III) could contribute to the regeneration of the Fenton active species, Fe^{2+}, driven by the electromotive force (*i.e.* $E_0 = 0.434$ V) (equation 8), just as V(III) worked in V-doped magnetite (Liang *et al.*, 2010a, 2010b, 2013).

$$V^{III}_{surf} + H_2O_2 \rightarrow V^{IV}_{surf} + \cdot OH + OH^-, \quad E_0 = 0.962 \text{ V (at pH = 3)} \qquad (7)$$

$$V^{III}_{surf} + Fe^{3+}_{aq} \rightarrow V^{IV}_{surf} + Fe^{2+}_{aq}, \; E_0 = 0.434 \text{ V (}vs\text{. NHE)} \qquad (8)$$

Impact of pH on the Fenton effects of H_2-treated samples

The pH is a very important factor in the Fenton reaction. Comparison of experiments with H_2-1173 and with an untreated rutile sample were conducted at different pH levels, ranging from 3.0 to 6.0 (Figure 7a). H_2-1173 and H_2-1073 showed the greatest MB removal rate at pH = 3.0, which was much greater than that of untreated rutile and other temperature-treated samples. The remarkable degrading rate of MB when H_2-1173 was added conformed to the pseudo-first order law with an apparent rate constant k = 1.4609 h^{-1} (fitted line shown in inset of Figure 7b). As the pH increased to 3.7, however, the MB removal rate of H_2-1173 was reduced significantly, to 30.3%. This unsatisfactory degrading result could be attributed to non-homogeneous catalysis due to the rapidly decreased concentration of leached Fe^{2+} ions, the activity of which was far less than homogeneous catalysis (Chou *et al.*, 2001; Liang *et al.*, 2010). The approximately linear correlations between the MB removal rate and the reaction time indicated that the reactions involved

Table 4. Concentration of dissolved Fe^{2+} and total Fe ions for untreated rutile and H_2-1173.

Sample	Total Fe (mg/L)	Fe^{2+} (mg/L)	Calculated Fe^{3+} (mg/L)
H_2-1173	1.51(±0.009)	1.30(±0.036)	0.21
Untreated rutile	0.36(±0.047)	0.32(±0.099)	0.04
Blank	0.022(±0.002)	bd	0.022

Notes: The concentration data were measured by 1,10-phenanthroline after 0.5 h of reaction at pH 3.0, in the absence of MB and H_2O_2. Numbers in parentheses are standard deviation uncertainties. 'bd' means below the detection limit of 0.02 mg/L.

https://doi.org/10.1346/CCMN.2018.064091 Published online by Cambridge University Press

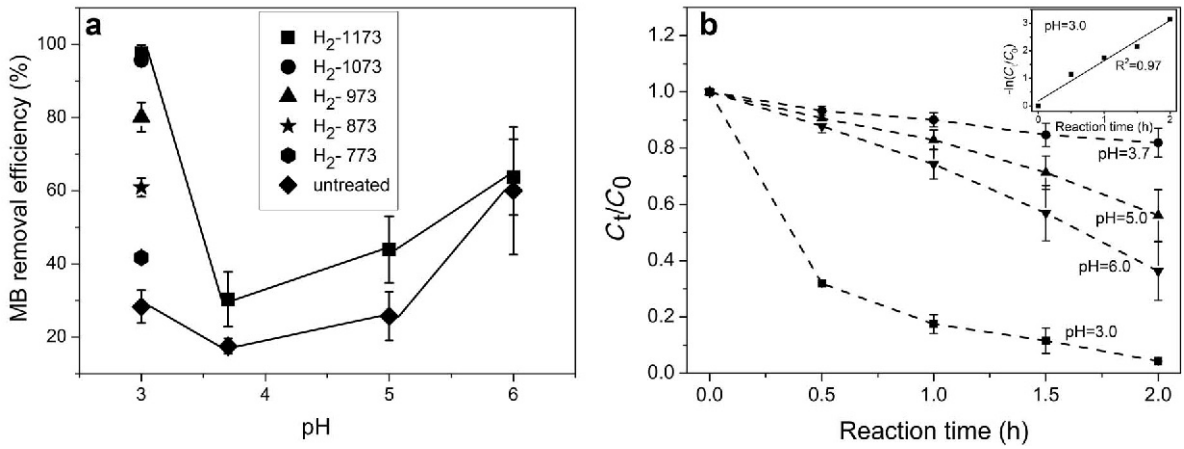

Figure 7. (a) Impact of pH on the Fenton reaction of the H_2-1173 sample and untreated rutile by degrading MB after 2 h. (b) MB removal rate of H_2-1173 corresponding to various pH values as a function of reaction time. Inset: fitted by pseudo-first order rate law at pH = 3.0, where the correlation coefficient $R^2 = 0.97$.

might follow a zero-order kinetics law ($R^2 = 0.98$, not shown). Physical adsorption, therefore, might play a vital role because, in this situation, the reaction rate depended only on the concentration of the substance adsorbed or adsorption sites but had nothing to do with MB concentration. Whether the pH was set at 5.0 or 6.0, H_2-1173 and untreated rutile kept the same trends of enhanced MB removal rate (Figure 7a,b). These performances may be ascribed to the physical adsorption and/or heterogeneous Fenton reaction involving surface bonding of Fe and V, as efficient homogeneous Fenton catalysis was impossible due to the lack of dissolved cations. In these two cases, the increasingly quick reaction rate happened after 1 h, suggesting that two reactions were involved, *i.e.* a physical reaction followed by a chemical reaction, conforming exactly to the characteristics of heterogeneous catalysis which usually exhibits activity in neutral pH conditions (Liang *et al.*, 2010; Pereira *et al.*, 2012; Liang *et al.*, 2013). The best performance in terms of eliminating a pollutant in strong acidic conditions means that natural rutile and its treated samples have the potential to solve extreme environmental problems. The material used in the present study, *i.e.* natural rutile and hydrogen-treated rutile, might also suggest other natural minerals to be used in the same way to deal with environmental problems.

GEOLOGICAL IMPLICATIONS

Natural rutile has been suggested to exist on Earth since the era of planetary accretion (>4.55 Ga) (Hazen *et al.*, 2008). Besides, rutile has been identified in Martian regolith and in the subsurface at an abundance of 0.5–2 wt.% (Baird *et al.*, 1976; Rieder *et al.*, 1997; Ming *et al.*, 2008). On inanimate Mars, the enrichment of reactive oxygen species (ROSs), *e.g.* hydroxyl radical (·OH) or superoxide radical ($\cdot O_2$), is assumed to be the main cause of 'lifelessness' because of destructive effects on organic matter (Lasne *et al.*, 2016). Deep insight into the formation pathways of ROSs and their reactivity on Mars, therefore, is central to understanding prebiotic biochemistry and this will also be helpful in the exploration and preservation of biomarkers. The remarkable role of TiO_2 in the photocatalytic formation and accumulation of ROSs when commercially synthetic TiO_2 was used as a reactant was described by Zent *et al.* (2008). Natural rutile must be imperfect with non-stoichiometry and impurities (such as substitutional Fe and V) in the actual geological circumstance in question, *e.g.* in Martian soil; this will distinguish it from synthetic, purchased TiO_2 which has fewer lattice defects. More importantly, the valence of V in Martian melt and minerals was suggested as a mixture of both V(III) and V(IV), while Fe(II) and Fe(III) were both likely species of Fe which vary with oxygen fugacity (Papike *et al.*, 2005; Karner *et al.*, 2006). As a result, to construct more analogous Martian surroundings in the laboratory on Earth, natural rutiles with low valence states of cations, like H_2-973, H_2-1073, and H_2-1173, rather than a commercial rutile, are probably better raw materials. On the other hand, a trace of H_2O_2 was observed directly in the Martian atmosphere and with a global average mixing ratio ranging from 18 to 32 ppb; this can penetrate up to hundreds of meters into the regolith (Bullock *et al.*, 1994; Zent, 1998; Clancy *et al.*, 2004; Encrenaz *et al.*, 2004). Consequently, the interaction between natural rutile and H_2O_2 in the form of the Fenton effect, as is presented in this work, should be a considerable pathway to produce ROSs; this, however, was not mentioned or was ignored in previous studies of Mars. In the present work, rutile samples with V(III), V(IV), Fe(II), and Fe(III) as foreign impurities (namely H_2-973, H_2-1073, and H_2-1173) exhibited a quite striking ability to eliminate MB molecules compared with commercial P25-TiO_2, which provided another potential and efficient pathway to generate strong

https://doi.org/10.1346/CCMN.2018.064091 Published online by Cambridge University Press

oxidizing ·OH and impact on the prebiotic biogeochemistry process.

CONCLUSIONS

In the present study, the influences of the chemical states of Fe and V on the Fenton reaction activity of a natural rutile sample were investigated. By hydrogen annealing from 773 K to 1173 K, the surface Fe(II) increased due to hydrogen reduction and the migration of bulk Fe to the surface by the heating effect. At the same time, V experienced reduction from V(V) to V(III) but, compared to Fe, favored remaining in the bulk lattice. As a result, the modified rutile samples displayed substantially increased MB removal rate due to the homogeneous Fenton effect of dissolved Fe^{2+}, physical adsorption, and heterogeneous Fenton effect of V(III). In addition, the efficiency and mechanism of MB degradation depended heavily on pH. Strong acidic conditions were beneficial to homogeneous Fenton catalysis, while faintly acid and neutral conditions favored physical adsorption and a heterogeneous Fenton reaction, respectively. The V and Fe co-doped rutile, in particular with low valence state cations, may promote the Fenton catalytic activity. The present study verified the Fenton effect of natural Fe- and V-bearing rutile and identified the crucial roles of V and Fe with different valence states. This could stimulate inspiration to utilize natural minerals and provide strategies for modifying minerals in the field of environmental science. The present research presents a novel pathway to ·OH generation, which might have happened or be happening on barren and lifeless Mars.

ACKNOWLEDGMENTS

The authors acknowledge support from the National Key Basic Research Program of China (973 Program, Grant No. 2014CB846001) and the National Natural Science Foundation of China (Grant No. 41522201 & 41230103). Prof J.H. Su, of the University of Science and Technology of China, is thanked for providing helpful suggestions in relation to the EPR spectra analysis.

REFERENCES

Allen, B.L. and Hajek, B.F. (1989) Mineral occurrence in soil environments. *Mammal Review*, **28**, 1–52.

Amorelli, A., Evans, J.C., Rowlands, C.C., and Egerton, T.A. (1987) An electron spin resonance study of rutile and anatase titanium dioxide polycrystalline powders treated with transition-metal ions. *Journal of the Chemical Society, Faraday Transactions 1: Physical Chemistry in Condensed Phases*, **83**, 3541–3548.

Baird, A.K., Clark, B.C., Jr, R.H., Keil, K., Christian, R.P., and Gooding, J.L. (1976) Mineralogic and petrologic implications of Viking geochemical results from Mars: interim report. *Science*, **194**, 1288–1293.

Bhattacharyya, K., Varma, S., Tripathi, A.K., Bharadwaj, S.R., and Tyagi, A.K. (2008) Effect of vanadia doping and its oxidation state on the photocatalytic activity of TiO_2 for gas-phase oxidation of ethene. *The Journal of Physical Chemistry C*, **112**, 19102–19112.

Bossmann, S.H., Oliveros, E., Göb, S., Siegwart, S., Dahlen, E.P., Payawan, L., Straub, J.M., Wörner, M., and Braun, A.M. (1998) New evidence against hydroxyl radicals as reactive intermediates in the thermal and photochemically enhanced Fenton reactions. *The Journal of Physical Chemistry A*, **102**, 5542–5550.

Brückner, A. (2006) Spin–spin exchange in vanadium-containing catalysts studied by in situ EPR: a sensitive monitor for disorder-related activity. *Topics in Catalysis*, **38**, 133–139.

Bullock, M.A., Stoker, C.R., Mckay, C.P., and Zent, A.P. (1994) A coupled soil-atmosphere model of H_2O_2 on Mars. *Icarus*, **107**, 142–154.

Cavani, F., Centi, G., Foresti, E., and Trifir, F. (1988) Surface structure and reactivity of vanadium oxide supported on titanium dioxide. V_2O_5/TiO_2 (rutile) catalysts prepared by hydrolysis. *Journal of the Chemical Society, Faraday Transactions 1: Physical Chemistry in Condensed Phases*, **84**, 237–254.

Chakradhar, R.P.S., Yasoda, B., Rao, J.L., and Gopal, N.O. (2006) Mixed alkali effect in Li_2O-Na_2O-B_2O_3, glasses containing Fe_2O_3 – an EPR and optical absorption study. *Materials Research Bulletin*, **41**, 1646–1656.

Chou, S., Huang, C., and Huang, Y.H. (2001) Heterogeneous and homogeneous catalytic oxidation by supported γ-FeOOH in a fluidized-bed reactor: kinetic approach. *Environmental Science & Technology*, **35**, 1247–1251.

Chuan, X.Y., Lu, A.H., Chen, J., Li, N., and Guo, Y.J. (2008) Microstructure and photocatalytic activity of natural rutile from China for oxidation of methylene blue in water. *Mineralogy and Petrology*, **93**, 143–152.

Clancy, R.T., Sandor, B.J., and Moriarty-Schieven, G.H. (2004) A measurement of the 362 GHz absorption line of Mars atmospheric H_2O_2. *Icarus*, **168**, 116–121.

Dolcater, D.L., Syers, J.K., and Jackson, M.L. (1970) Titanium as free oxide and substituted forms in kaolinites and other soil minerals. *Clays and Clay Minerals*, **18**, 71–79.

Dong, Y., Chen, S., Zhang, X., Yang, J., Liu, X., and Meng, G. (2006) Fabrication and characterization of low cost tubular mineral-based ceramic membranes for micro-filtration from natural zeolite. *Journal of Membrane Science*, **281**, 592–599.

Egerton, T.A., Harris, E., John Lawson, E., Mile, B., and Rowlands, C.C. (2001) An EPR study of diffusion of iron into rutile. *Physical Chemistry Chemical Physics*, **3**, 497–504.

Encrenaz, T., Bezard, B., Greathouse, T.K., Richter, M.J., Lacy, J.H., Atreya, S.K., Wong, A.S., Lebonnois, S., Lefevre, F., and Forget, F. (2004) Hydrogen peroxide on Mars: evidence for spatial and seasonal variations. *Icarus*, **170**, 424–429.

Fiedor, J.N., Bostick, W.D., Jarabek, R.J., and Farrell, J. (1998) Understanding the mechanism of uranium removal from groundwater by zero-valent iron using X-ray photoelectron spectroscopy. *Environmental Science & Technology*, **32**, 1466–1473.

Fujii, T., De Groot, F.M.F., Sawatzky, G.A., Voogt, F.C., Hibma, T., and Okada, K. (1999) In situ XPS analysis of various iron oxide films grown by NO_2-assisted molecular-beam epitaxy. *Physical Review B*, **59**, 3195–3202.

Gallay, R., Van der Klink, J.J., and Moser, J. (1986) EPR study of vanadium (4+) in the anatase and rutile phases of TiO_2. *Physical Review B*, **34**, 3060–3068.

Geng, B., Jin, Z., Li, T., and Qi, X. (2009) Preparation of chitosan-stabilized Fe(0) nanoparticles for removal of hexavalent chromium in water. *Science of the Total Environment*, **407**, 4994–5000.

Gómez-Hortigüela, L., Pinar, A.B., Pérez-Pariente, J., Sani, T.,

Chebude, Y., and Díaz, I. (2014) Ion-exchange in natural zeolite stilbite and significance in defluoridation ability. *Microporous and Mesoporous Materials*, **193**, 93–102.

Gopal, N.O., Narasimhulu, K.V., and Rao, J.L. (2004) EPR, optical, infrared and Raman spectral studies of actinolite mineral. *Spectrochimica Acta Part A: Molecular and Biomolecular Spectroscopy*, **60**, 2441–2448.

Griffin, R.A., Au, A., and Frost, R.R. (1977) Effect of pH on adsorption of chromium from landfill leachate by clay minerals. *Journal of Environmental Science & Health Part A – Environmental Science & Engineering*, **12**, 431–449.

Gülay, A., Tatari, K., Musovic, S., Mateiu, R.V., Albrechtsen, H.J., and Smets, B.F. (2014) Internal porosity of mineral coating supports microbial activity in rapid sand filters for groundwater treatment. *Applied and Environmental Microbiology*, **80**, 7010–7020.

Hazen, R.M., Papineau, D., Leeker, W.B., Downs, R.T., Ferry, J.M., McCoy, T.J., Sverjensky, D.A., and Yang, H.X. (2008) Mineral evolution. *American Mineralogist*, **93**, 1693–1720.

Jackson, M.L., Tyler, S.A., Willis, A.L., Bourbeau, G.A., and Pennington, R.P. (1948) Weathering sequence of clay-size minerals in soils and sediments. I. Fundamental generalizations. *The Journal of Physical Chemistry*, **52**, 1237–1260.

Karner, J.M., Sutton, S.R., Papike, J.J., Shearer, C.K., Jones, J.H., and Newville, M. (2006) Application of a new vanadium valence oxybarometer to basaltic glasses from the Earth, Moon, and Mars. *American Mineralogist*, **91**, 270–277.

Kera, Y. and Matsukaze, Y. (1986) Dynamical change in the crystal field around the V (IV) ion on titanium dioxide (rutile) surface accompanied by the interaction with adsorbed oxygen molecules. *The Journal of Physical Chemistry*, **90**, 5752–5755.

Klosek, S. and Raftery, D. (2001) Visible light driven V-doped TiO_2 photocatalyst and its photooxidation of ethanol. *The Journal of Physical Chemistry B*, **105**, 2815–2819.

Knapp, M.J., Krzystek, J., Brunel, L.C., and Hendrickson, D.N. (2000) High-frequency EPR study of the ferrous ion in the reduced rubredoxin model $[Fe(SPh)_4]_2$. *Inorganic Chemistry*, **39**, 281–288.

Kremer, M.L. (2008) Kinetics of aerobic and anaerobic oxidations of ethanol by Fenton's reagent. *International Journal of Chemical Kinetics*, **40**, 541–553.

Laiju, A.R., Sivasankar, T., and Nidheesh, P.V. (2014) Iron-loaded mangosteen as a heterogeneous Fenton catalyst for the treatment of landfill leachate. *Environmental Science and Pollution Research*, **21**, 10900–10907.

Lasne, J., Noblet, A., Szopa, C., Navarro-González, R., Cabane, M., Poch, O., Stalport, F., François, P., Atreya, S.K., and Coll, P. (2016) Oxidants at the surface of Mars: a review in light of recent exploration results. *Astrobiology*, **16**, 977.

Li, Y., Li, Y., Yin, Y., Xia, D., Ding, H., Ding, C., Wu, J., Yan, Y., Liu, Y., Chen, N., Wong, P.K., and Lu, A. (2018) Facile synthesis of highly efficient $ZnO/ZnFe_2O_4$ photocatalyst using earth-abundant sphalerite and its visible light photocatalytic activity. *Applied Catalysis B: Environmental*, **226**, 324–336.

Liang, X., Zhu, S., Zhong, Y., Zhu, J., Yuan, P., He, H., and Zhang, J. (2010a) The remarkable effect of vanadium doping on the adsorption and catalytic activity of magnetite in the decolorization of methylene blue. *Applied Catalysis B Environmental*, **97**, 151–159.

Liang, X., Zhong, Y., Zhu, S., Zhu, J., Yuan, P., He, H., and Zhang, J. (2010b) The decolorization of Acid Orange II in non-homogeneous Fenton reaction catalyzed by natural vanadium–titanium magnetite. *Journal of Hazardous Materials*, **181**, 112–120.

Liang, X., He, Z., Zhong, Y., Tan, W., He, H., Yuan, P., Zhu, J., and Zhang, J. (2013) The effect of transition metal substitution on the catalytic activity of magnetite in heterogeneous Fenton reaction: in interfacial view. *Colloids and Surfaces A: Physicochemical and Engineering Aspects*, **435**, 28–35.

Lu, A., Liu, J., Zhao, D., Guo, Y., Li, Q., and Li, N. (2004) Photocatalysis of V-bearing rutile on degradation of halohydrocarbons. *Catalysis Today*, **90**, 337–342.

Lu, A., Li, Y., Lv, M., Wang, C., Yang, L., Liu, J., Wang Y., Wong, K.H., and Wong, P.K. (2007) Photocatalytic oxidation of methyl orange by natural V-bearing rutile under visible light. *Solar Energy Materials & Solar Cells*, **91**, 1849–1855.

Lu, A., Li, Y., Jin, S., Wang, X., Wu, X.L., Zeng, C., Li, Y, Ding, H., Hao, R., Lv, M., Wang, C., Tang, Y., and Dong, H. (2012) Growth of non-phototrophic microorganisms using solar energy through mineral photocatalysis. *Nature Communications*, **3**, 768.

Luo, Z., Lu, A., Li, Y., Zhuang, W., Wu, J., Qin, S., and Wang, C. (2012) Enhanced visible-light response of natural V-bearing rutile by annealing under argon. *European Journal of Mineralogy*, **24**, 551–557.

Matta, R., Hanna, K., Kone, T., and Chiron, S. (2008) Oxidation of 2,4,6-trinitrotoluene in the presence of different iron-bearing minerals at neutral pH. *Chemical Engineering Journal*, **144**, 453–458.

Mehmood, A., Akhtar, M.S., Deng, Y., Dixon, J.B., Imran, M., and Rukh, S. (2015) Iron oxide minerals in soils derived from different parent materials. *International Journal of Plant and Soil Science*, **5**, 110–116.

Ming, D.W., Gellert, R., Morris, R.V., Arvidson, R.E., Brückner, J., Clark, B.C., Cohen, B.A., d'Uston, C., Economou, T., Fleischer, I., Klingelhöfer, G., McCoy, T.J., Mittlefehldt, D.W., Schmidt, M.E., Schröder, C., Squyres, S.W., Tréguier, E., Yen, A.S., and Zipfel, J. (2008) Geochemical properties of rocks and soils in Gusev Crater, Mars: results of the Alpha Particle X-ray spectrometer from Cumberland Ridge to Home Plate. *Journal of Geophysical Research*, **113**, E12S39.

Occhiuzzi, M., Cordischi, D., and Dragone, R. (2003) Manganese ions in the monoclinic, tetragonal and cubic phases of zirconia: an XRD and EPR study. *Physical Chemistry Chemical Physics*, **5**, 4938–4945.

Papike, J.J., Karner, J.M., and Shearer, C.K. (2005) Comparative planetary mineralogy: Valence state partitioning of Cr, Fe, Ti, and V among crystallographic sites in olivine, pyroxene, and spinel from planetary basalts. *36th Annual Lunar and Planetary Science Conference* (Vol. 36). 36th Annual Lunar and Planetary Science Conference.

Pecchi, G., Reyes, P., Lopez, T., Gomez, R., Moreno, A., Fierro, J.L.G., and Martínez-Arias, A. (2003) Catalytic combustion of methane on Fe-TiO_2 catalysts prepared by sol-gel method. *Journal of Sol-Gel Science and Technology*, **27**, 205–214.

Pereira, M.C., Oliveira, L.C.A., and Murad, E. (2012) Iron oxide catalysts: Fenton and Fenton-like reactions – a review. *Clay Minerals*, **47**, 285–302.

Pignatello, J.J., Oliveros, E., and MacKay, A. (2006) Advanced oxidation processes for organic contaminant destruction based on the Fenton reaction and related chemistry. *Critical Reviews in Environmental Science and Technology*, **36**, 1–84.

Rieder, R., Economou, T., Wanke, H., Turkevich, A., Crisp, J., Bruckner, J., Dreibus, G., and McSween, H.Y. (1997) The chemical composition of Martian soil and rocks returned by the mobile alpha proton X-ray spectrometer: preliminary results from the X-ray mode. *Science*, **278**, 1771–1774.

Rodella, C.B., Franco, R.W., Magon, C.J., Donoso, J.P.,

Nunes, L.A., Saeki, M.J., Aegerter, M.A., Sargentelli, A., and Florentino, A.O. (2002) V_2O_5/TiO_2 catalytic xerogels Raman and EPR studies. *Journal of Sol-Gel Science and Technology*, **25**, 83–88.

Sawatzky, G.A. and Post, D. (1979) X-ray photoelectron and Auger spectroscopy study of some vanadium oxides. *Physical Review B*, **20**, 1546.

Sayin, M. (1975) Anatase and rutile determination in kaolinite deposits. *Clays and Clay Minerals*, **23**, 437–443.

Seki, M., Akther Hossain, A.K.M., Kawai, T., and Tabata, H. (2005) High-temperature cluster glass state and photomagnetism in Zn- and Ti-substituted $NiFe_2O_4$ films. *Journal of Applied Physics*, **97**, 516.

Shi, L., Dong, H., Reguera, G., Beyenal, H., Lu, A., Liu, J., Yu, H.Q., and Fredrickson, J.K. (2016) Extracellular electron transfer mechanisms between microorganisms and minerals. *Nature Reviews Microbiology*, **14**, 651–662.

Shimizu, A., Tokumura, M., Nakajima, K., and Kawase, Y. (2012) Phenol removal using zero-valent iron powder in the presence of dissolved oxygen: roles of decomposition by the Fenton reaction and adsorption/precipitation. *Journal of Hazardous Materials*, **201**, 60–67.

Soria, J., Conesa, J.C., Augugliaro, V., Palmisano, L., Schiavello, M., and Sclafani, A. (1991) Dinitrogen photoreduction to ammonia over titanium dioxide powders doped with ferric ions. *Cheminform*, **22**, 274–282.

Suzuki, Y. and Pavasupree, S. (2005) Natural rutile-derived titanate nanofibers prepared by direct hydrothermal processing. *Journal of Materials Research*, **20**, 1063–1070.

Tekbaş, M., Yatmaz, H.C., and Bektaş, N. (2008) Heterogeneous photo-Fenton oxidation of reactive azo dye solutions using iron-exchanged zeolite as a catalyst. *Microporous and Mesoporous Materials*, **115**, 594–602.

Trifir, F. (1998) The chemistry of oxidation catalysts based on mixed oxides. *Catalysis Today*, **41**, 21–35.

Thorp, J.S. and Eggleston, H.S. (1985) Rhombic symmetry sites in Fe/TiO_2 powders. *Journal of Materials Science Letters*, **4**, 1140–1142.

Tian, B., Li, C., Gu, F., Jiang, H., Hu, Y., and Zhang, J. (2009) Flame sprayed V-doped TiO_2 nanoparticles with enhanced photocatalytic activity under visible light irradiation. *Chemical Engineering Journal*, **151**, 220–227.

Uddin, M.K. (2017) A review on the adsorption of heavy metals by clay minerals, with special focus on the past decade. *Chemical Engineering Journal*, **308**, 438–462.

Wagner, C.D. (1979) *Handbook of X-ray photoelectron spectroscopy*. Perkin-Elmer.

Wagner, C.D. (1983) Sensitivity factors for XPS analysis of surface atoms. *Journal of Electron Spectroscopy and Related Phenomena*, **32**, 99–102.

Wang, C., Hong, H., Li, Z., Yin, K., Xie, J., Liang, G., Song, B., Song, E., and Zhang, K. (2013) The Eocene–Oligocene climate transition in the Tarim Basin, northwest China: evidence from clay mineralogy. *Applied Clay Science*, **74**, 10–19.

Wang, S. (2008) A comparative study of Fenton and Fenton-like reaction kinetics in decolourisation of wastewater. *Dyes and Pigments*, **76**, 714–720.

Xia, D., Ng, T.W., An, T., Li, G., Li, Y., Yip, H.Y., Zhao, J., Lu, A., and Wong, P.K. (2013) A recyclable mineral catalyst for visible-light-driven photocatalytic inactivation of bacteria: natural magnetic sphalerite. *Environmental Science & Technology*, **47**, 11166–11173.

Xia, D., Yin, R., Sun, J., An, T., Li, G., Wang, W., Zhao, H., and Wong, P.K. (2017) Natural magnetic pyrrhotite as a high-efficient persulfate activator for micropollutants degradation: Radicals identification and toxicity evaluation. *Journal of Hazardous Materials*, **340**, 435–444.

Yamashita, T. and Hayes, P. (2008) Analysis of XPS spectra of Fe^{2+} and Fe^{3+} ions in oxide materials. *Applied Surface Science*, **254**, 2441–2449.

Zent, A.P. (1998) On the thickness of the oxidized layer of the Martian regolith. *Journal of Geophysical Research Planets*, **103**, 31491–31498.

Zent, A.P., Ichimura, A.S., Quinn, R.C., and Harding, H.K. (2008) The formation and stability of the superoxide radical (O_2^-) on rock-forming minerals: band gaps, hydroxylation state, and implications for mars oxidant chemistry. *Journal of Geophysical Research Planets*, **113**, 102–110.

(*Received 30 November 2017; revised 21 March 2018; Ms 1241; AE: Chun-Hui Zhou*)